



Experimental and theoretical investigations on piezoelectric-based energy harvesting from bridge vibrations under travelling vehicles



M. Karimi, A.H. Karimi, R. Tikani*, S. Ziaei-Rad

Department of Mechanical Engineering, Isfahan University of Technology, Isfahan 84156-83111, Iran

ARTICLE INFO

Keywords:

Energy harvesting
Structural health monitoring
Piezoelectric
Bridges

ABSTRACT

This paper aims to investigate the amount of energy which can be harvested by a cantilever beam type piezoelectric energy harvester from a bridge vibration. The sources of vibration are vehicles traversing the bridge. Two types of masses are considered as models for traversing vehicles: concentrated and distributed masses. The mass of the harvester is assumed negligible compared to that of the bridge. First, the problem of moving mass travelling with a constant speed over a beam is considered. The formulations for both concentrated and distributed masses are presented. The obtained results are then compared to the data available in the literature, in order to validate the model of a beam with a moving mass. Next, a mathematical model for the harvester is proposed, which is composed of an Euler–Bernoulli beam as a substrate, a tip mass, and a single piezoelectric patch whose electrodes are connected to a changeable resistance. To validate the model, the harvester is fabricated and tested on a shaker. The electroelastic frequency response functions of the system are measured by low-amplitude chirp excitation tests. The optimal resistive load at the resonance frequency, obtained from theory and experiments, are compared. Finally, the acceleration time histories for the beam at mid-span, where the harvester is located, are calculated for two mass types and used as base excitation signals to the harvester. These signals are replayed on an electromagnetic shaker to simulate the bridge vibrations on the fabricated harvester and the experimental results are compared with theoretical ones. Good agreement is observed.

1. Introduction

Bridges play an undeniable role in ground transportation systems. Monitoring the health of civil infrastructures, such as bridges is a way, often used in order to prevent hazards from their degradation. Structural Health Monitoring (SHM) systems, which keep civil infrastructures safer and more durable, have become widely popular in the last decade [1,2]. Furthermore, Wireless Sensor Networks (WSNs), which are able to make SHM systems more efficient, have attracted significant attention recently. These networks not only solve a number of issues with traditional wired sensor grids, such as lack of flexibility, necessity of repairing damaged cables, and changing configurations, but also they are quite affordable, can be easily implemented, need easier maintenance, increase the density of located sensors, and have a good ability to be applied to bridge infrastructures [3].

Power consumption is one of the main challenging dilemmas which WSNs encounter with. According to the simplest definition reported in the literature, the lifetime of a sensor network is the time span from the instant the network starts operating to the failure of first sensor node

[4]. Meanwhile, lifetime of a sensor node has a strong dependence on the nodes' battery lifetime. Historically, small alkaline batteries had long been utilized as power supply in wireless sensor nodes owing to their high energy density and long shelf life. However, they are flawed in that they contain toxic substances and emit corrosive gases. In addition, these batteries have finite power supply and hence a short operational life due to compact size of wireless sensor nodes. As a result, batteries can be eliminated or at least made self-rechargeable [5].

Among different forms of energy that can be converted to electric energy, kinetic energy is an appropriate choice for environments which are rich in vibrations [6]. The lost energy of bridge vibrations caused by moving vehicles can be converted to electric energy by vibration energy harvesters. However, their application on bridge infrastructures has not been completely studied yet. In addition, in and of itself, the amount of harvested energy can be used to detect the presence of damage; thus, a shift in the amount of scavenged energy may be an indication of a change in the conditions of the bridge caused by damage [7]. Among different kinds of mechanisms for harvesting energy from

* Corresponding author.

E-mail address: r_tikani@cc.iut.ac.ir (R. Tikani).

vibrations, including piezoelectric, electromagnetic, and electrostatic, piezoelectric-based energy harvesting is a promising choice due to its high energy density, compact dimensions, and simplicity of application [8].

A number of studies have been reported on energy harvesting in bridge infrastructures. A feasibility study in this field was performed by Williams et al. [9]. They applied measured vibrational responses data taken on two common bridges as excitations to a theoretical model of an inductive generator and determined the power output, which was found to be sufficient for powering an acceleration sensor. Considering a highway bridge model under a moving point force as the source of energy which can be harvested, Ali et al. [10] theoretically estimated the maximum power that a linear single-degree-of-freedom piezoelectric energy harvester model can scavenge. The authors reported their results for two types of harvesting circuits: with and without inductor. However, any device fabrication and real time experimentation were not performed. Galchev et al. [11] fabricated an electromagnetic inertial power harvester and tested its performance along the length of a suspension bridge. The device generated a mean power of approximately 0.5–0.75 μ W without adjusting at each bridge location. Analyzing the in situ acceleration measurements of a particular concrete highway bridge, Peigney and Siegert [12] designed a prototype of a cantilever piezoelectric harvester. They modeled and tested their harvester on the bridge and reported an average power output of about 0.3 mW. Ye Zhang et al. [13] examined piezoelectric energy harvesting with cantilever beam configuration on four concrete bridge platforms. They simulated three-dimensional bridges with HS20-44 truck models by using ANSYS and MATLAB. The harvester energy output was found to increase with poorer road conditions and bridges with smaller span lengths.

This paper aims to investigate the amount of energy which can be harvested from bridge infrastructures undergoing moving vehicles by piezoelectric-based energy harvesters. To this end, two types of masses as traversing vehicle models are considered namely concentrated and distributed. Comparing the deflection time histories of a specified point of the bridge under a moving part with and without consideration of its inertial effects reveals that neglecting these effects can lead to gross errors particularly for heavy masses and those with high speeds [14]. Thus, in this study, the model of moving point force is substituted by the moving concentrated mass one, which is more realistic in modeling the moving vehicle over the bridge due to acceleration components of it, whereas in the previous similar works, in the case of energy harvesting, they were neglected. Furthermore, since no point mass exists physically, the problem of the moving concentrated mass on a beam is extended to that of the moving distributed mass to enhance the reality of problem formulation. In this problem, similar to the moving concentrated mass one, all inertial effects of moving body are taken into account. The application of such an analysis also can be the investigation of energy harvesting from a bridge under a travelling train. Next, the mass of the harvester is assumed negligible compared to that of the bridge. Thus, first, the moving mass problems are solved. Subsequently, the vibrations of a particular point on the bridge are given to a validated model of the harvester as the base excitations, theoretically. Furthermore, the acceleration signals derived by solving the moving mass problems are replayed on an electromagnetic shaker to simulate the bridge vibrations on the fabricated harvester and the experimental results are compared with theoretical ones.

2. Bridge-vehicle interaction model

A steady state solution does not exist for the dynamic response of distributed system undergoing moving masses. In order to precisely determine the dynamic response of a beam under moving masses, their inertial effects should be taken into account, particularly for heavy masses and high speeds. In this section, first, the governing equation of the motion of an Euler-Bernoulli beam with hinged-hinged boundary

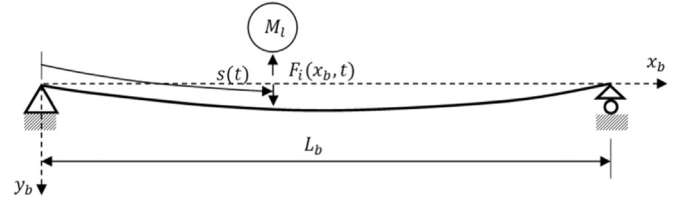


Fig. 1. Schematic diagram of an Euler-Bernoulli beam under a moving concentrated mass.

conditions under a moving concentrated mass with a constant speed is derived. Next, the governing equations of motion are developed for a moving distributed mass with a constant velocity.

2.1. Vibration of the underlying structure under a moving concentrated mass

Generally, the equation of motion for a beam of length L_b , subjected to N concentrated moving masses, can be written as:

$$m_b \frac{\partial^2 w(x_b, t)}{\partial t^2} + C_b \frac{\partial w(x_b, t)}{\partial t} + E_b I_b \frac{\partial^4 w(x_b, t)}{\partial x_b^4} = \sum_{i=1}^N F_i(x_b, t) \delta(x_b - s(t)) \quad (1)$$

where $w(x_b, t)$ is the transverse deflection of the beam at point x_b and time t . Parameters m_b , C_b , E_b and I_b are mass per unit length, viscous damping coefficient, linear elastic modulus, and the area moment of inertia of the cross section of the beam, respectively. $F_i(x_b, t)$ is the interaction forcing function due to the motion and location of the i th moving mass, and consists of weight and inertial forces of the moving mass. $\delta(x_b - s(t))$ is the Dirac delta function, where $s(t)$ is the instantaneous position of the moving mass from the left boundary (see Fig. 1).

In this investigation we will consider a simplified case of single moving mass M_i , moving with a constant velocity. Thus, the governing equation of motion by using Newton's second law and considering weight and inertial forces of the moving mass will reduce to:

$$m_b \frac{\partial^2 w(x_b, t)}{\partial t^2} + C_b \frac{\partial w(x_b, t)}{\partial t} + E_b I_b \frac{\partial^4 w(x_b, t)}{\partial x_b^4} = M_i \left(g - \frac{\partial^2 w(x_b, t)}{\partial t^2} - s^2 \frac{\partial^2 w(x_b, t)}{\partial x_b^2} - 2s \frac{\partial^2 w(x_b, t)}{\partial x_b \partial t} \right) \delta(x_b - s(t)) \quad (2)$$

where g is the acceleration due to gravity and the dot symbol denotes the time derivatives so \dot{s} is the constant velocity of the moving mass. By using modal superposition followed by simplification of Eq. (2) according to the classical Galerkin method, the solution can be derived. For a simply supported beam, the displacement function, $w(x_b, t)$, from the first mode of vibration can be written as [15]:

$$w(x_b, t) = W(x_b) Q(t) \quad (3)$$

where $W(x_b)$ is the fundamental normalized mode shape function of a simply supported beam ($\sqrt{2}/m_b L_b \sin(\pi x_b / L_b)$) and $Q(t)$ is a function of time, t . By substituting Eq. (3) into Eq. (2) followed by multiplying both sides by $W(x_b)$, and integrating from 0 to L_b , we get:

$$M_e \ddot{Q} + C_e \dot{Q} + K_e Q = F_e \quad (4)$$

where the coefficient M_e , C_e , and K_e are termed as apparent mass, damping, and stiffness, respectively, and are defined as follows:

$$M_e = 1 + M_i A_1^2 \sin^2(\Omega t) \quad (5a)$$

$$C_e = 2\zeta_{1b} \omega_{1b} + M_i A_1^2 \Omega \sin(2\Omega t) \quad (5b)$$

$$K_e = \omega_{1b}^2 - M_i A_1^2 \Omega^2 \sin^2(\Omega t) \quad (5c)$$

where ω_{1b} is the fundamental frequency of a simply supported beam

$(\omega_{1b}=(\pi^2/L_b^2)\sqrt{E_b I_b/m_b})$ and ζ_{1b} is its first mode damping ratio. A_1 and Ω are defined as:

$$A_1 = \sqrt{\frac{2}{m_b L_b}} \tag{6}$$

$$\Omega = \frac{\pi \dot{s}}{L_b} \tag{7}$$

In Eq. (4), F_e is the generalized force associated with the generalized coordinate $Q(t)$, and is calculated as:

$$F_e = M_1 g A_1 \sin \Omega t \tag{8}$$

2.2. Vibration of the underlying structure under a partially distributed moving mass

Since no point mass exists physically, considering a load distribution interval for the moving mass is more realistic as compared with the moving point mass. Here, therefore, the problem of the moving concentrated mass on a beam is extended to that of the moving distributed mass. In addition, the moving distributed mass can be considered as the model of a train [16,17]. The length of the moving distributed mass is of importance, which divides the problem into the three separate steps. In each step, the governing equations of motion of the system are different. For a moving distributed mass shorter than the length of the beam, as shown in Fig. 2, step one occurs during the time it takes for the moving body to enter the beam completely. In other words, the left end of the moving part passes the first support. This is called the entrance step. The period of time during which the distributed mass is entirely located on the structure is the second step, called the main step. Lastly, from the time the moving body arrives to the second support until it departs from the beam is the last step, namely the exit step.

As shown in Fig. 2, the moving distributed mass is loaded by a distributed force $f(\lambda, t)$ which is directly resulted by the rigid interaction between the moving part and the structure. Therefore, the same displacement for both parts is an appropriate assumption. The moving body travels with a constant velocity, \dot{s} such that the front of the body with a coordinate shown by λ , is in the $s(t)$ position at each time t . In order to calculate $f(\lambda, t)$, it needs to find the equation of motion for the moving body. The relation between coordinates according to Fig. 2 is:

$$x_b = s(t) + \lambda \tag{9}$$

consequently, we have:

$$\frac{\partial w}{\partial \lambda} = \frac{\partial w}{\partial x_b} \tag{10}$$

By using Newton's second law and Eq. (10) for an element in x_b position, the governing equation of motion for the moving distributed mass can be obtained as follows:

$$m_d \frac{\partial^2 w(x_b, t)}{\partial t^2} = m_d \left(g - \dot{s}^2 \frac{\partial^2 w(x_b, t)}{\partial x_b^2} - 2\dot{s} \frac{\partial^2 w(x_b, t)}{\partial x_b \partial t} \right) - f(\lambda, t) \tag{11}$$

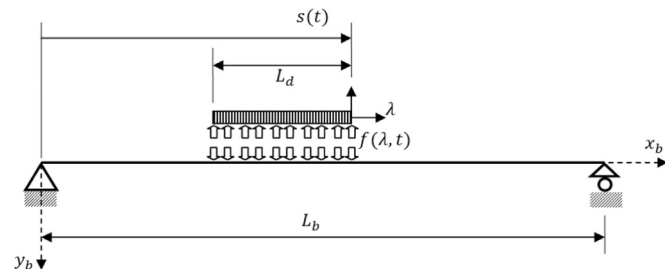


Fig. 2. Schematic diagram of an Euler-Bernoulli beam under a partially distributed moving mass.

where m_d is the mass per unit length of the moving distributed mass. In this study, the bending stiffness of the moving distributed mass is assumed to be zero. The equation of motion for the beam subjected to a moving distributed force is:

$$m_b \frac{\partial^2 w(x_b, t)}{\partial t^2} + C_b \frac{\partial w(x_b, t)}{\partial t} + E_b I_b \frac{\partial^4 w(x_b, t)}{\partial x_b^4} = f(\lambda, t) [U(0) - U(s(t))] \tag{12}$$

where $U(s(t))$ is the unit step function.

Step1: The entrance step.

Substituting $f(\lambda, t)$ from Eq. (11) into Eq. (12), the equation of motion for the entrance step can be rewritten as:

$$m_b \frac{\partial^2 w(x_b, t)}{\partial t^2} + C_b \frac{\partial w(x_b, t)}{\partial t} + E_b I_b \frac{\partial^4 w(x_b, t)}{\partial x_b^4} = m_d \left(g - \frac{\partial^2 w(x_b, t)}{\partial t^2} - \dot{s}^2 \frac{\partial^2 w(x_b, t)}{\partial x_b^2} - 2\dot{s} \frac{\partial^2 w(x_b, t)}{\partial x_b \partial t} \right) [U(0) - U(\dot{s}t)] \text{ for } 0 \leq t \leq \frac{L_d}{\dot{s}} \tag{13}$$

The only difference between Eq. (13), and Eq. (2) is the unit step function used instead of the Dirac delta function. For a moving distributed mass with a length larger than that of the beam, the equation of motion is the same but with different period of time.

By using a same solution approach, which explained for moving concentrated mass and considering only the first mode of the beam, we get:

$$M_{1e} \ddot{Q} + C_{1e} \dot{Q} + K_{1e} Q = F_{1e} \text{ for } 0 \leq t \leq \frac{L_d}{\dot{s}} \tag{14}$$

where

$$M_{1e} = 1 + \frac{1}{2} m_d A_1^2 \left(\dot{s}t - \frac{L_b}{2\pi} \sin(2\Omega t) \right) \tag{15a}$$

$$C_{1e} = 2\zeta_{1b} \omega_{1b} - \frac{1}{2} m_d A_1^2 \dot{s} (\cos(2\Omega t) - 1) \tag{15b}$$

$$K_{1e} = \omega_{1b}^2 - \frac{1}{2} m_d A_1^2 \dot{s}^2 \left(\frac{\pi}{L_b} \right)^2 \left(\dot{s}t - \frac{L_b}{2\pi} \sin(2\Omega t) \right) \tag{15c}$$

$$F_{1e} = m_d g A_1 \frac{L_b}{\pi} (1 - \cos(\Omega t)) \tag{15d}$$

Step2: The main step.

The equation of motion for the main step is as follows:

$$m_b \frac{\partial^2 w(x_b, t)}{\partial t^2} + C_b \frac{\partial w(x_b, t)}{\partial t} + E_b I_b \frac{\partial^4 w(x_b, t)}{\partial x_b^4} = m_d \left(g - \frac{\partial^2 w(x_b, t)}{\partial t^2} - \dot{s}^2 \frac{\partial^2 w(x_b, t)}{\partial x_b^2} - 2\dot{s} \frac{\partial^2 w(x_b, t)}{\partial x_b \partial t} \right) [U(\dot{s}t - L_d) - U(\dot{s}t)] \text{ for } \frac{L_d}{\dot{s}} \leq t \leq \frac{L_b}{\dot{s}} \tag{16}$$

It should be noted that the initial conditions in Step 2 are those obtained at the end of the entrance step. As before, in this step, a similar discrete equation of motion can be obtained, but with different coefficients and period of time as:

$$M_{2e} \ddot{Q} + C_{2e} \dot{Q} + K_{2e} Q = F_{2e} \text{ for } \frac{L_d}{\dot{s}} \leq t \leq \frac{L_b}{\dot{s}} \tag{17}$$

where

$$M_{2e} = 1 + \frac{1}{2} m_d A_1^2 \left\{ L_d + \frac{L_b}{2\pi} \left[\sin \left(2\Omega t - \frac{2\pi L_d}{L_b} \right) - \sin(2\Omega t) \right] \right\} \tag{18a}$$

$$C_{2e} = 2\zeta_{1b}\omega_{1b} - \frac{1}{2}m_d A_1^2 \dot{s} \left[\cos(2\Omega t) - \cos\left(2\Omega t - \frac{2\pi L_d}{L_b}\right) \right] \quad (18b)$$

$$K_{2e} = \omega_{1b}^2 - \frac{1}{2}m_d A_1^2 s^2 \left(\frac{\pi}{L_b} \right)^2 \left\{ L_d + \frac{L_b}{2\pi} \left[\sin\left(2\Omega t - \frac{2\pi L_d}{L_b}\right) - \sin(2\Omega t) \right] \right\} \quad (18c)$$

$$F_{2e} = m_d g A_1 \frac{L_b}{\pi} \left(\cos\left(\Omega t - \frac{\pi L_d}{L_b}\right) - \cos(\Omega t) \right) \quad (18d)$$

Step3: The exit step.

The equation of motion in this step is given below:

$$m_b \frac{\partial^2 w(x_b, t)}{\partial t^2} + C_b \frac{\partial w(x_b, t)}{\partial t} + E_b I_b \frac{\partial^4 w(x_b, t)}{\partial x_b^4} = m_d \left(g - \frac{\partial^2 w(x_b, t)}{\partial t^2} - s^2 \frac{\partial^2 w(x_b, t)}{\partial x_b^2} - 2s \frac{\partial^2 w(x_b, t)}{\partial x_b \partial t} \right) [U(st - L_d) - U(L_b)] \text{ for } \frac{L_b}{s} \leq t \leq \frac{L_b + L_d}{s} \quad (19)$$

It should be mentioned that the initial conditions in this step are those obtained at the end of Step 2. As in the two previous steps, we get:

$$M_{3e} \ddot{Q} + C_{3e} \dot{Q} + K_{3e} Q = F_{3e} \text{ for } \frac{L_b}{s} \leq t \leq \frac{L_b + L_d}{s} \quad (20)$$

where

$$M_{3e} = 1 + \frac{1}{2}m_d A_1^2 \left[L_d + L_b - st + \frac{L_b}{2\pi} \sin\left(2\Omega t - \frac{2\pi L_d}{L_b}\right) \right] \quad (21a)$$

$$C_{3e} = 2\zeta_{1b}\omega_{1b} - \frac{1}{2}m_d A_1^2 \dot{s} \left[1 - \cos\left(2\Omega t - \frac{2\pi L_d}{L_b}\right) \right] \quad (21b)$$

$$K_{3e} = \omega_{1b}^2 - \frac{1}{2}m_d A_1^2 s^2 \left(\frac{\pi}{L_b} \right)^2 \left[L_d + L_b - st + \frac{L_b}{2\pi} \sin\left(2\Omega t - \frac{2\pi L_d}{L_b}\right) \right] \quad (21c)$$

$$F_{3e} = m_d g A_1 \frac{L_b}{\pi} \left[\cos\left(\Omega t - \frac{\pi L_d}{L_b}\right) + 1 \right] \quad (21d)$$

3. Numerical solution to the moving mass problem

Eqs. (4), (14), (17), and (20) are ordinary differential equations with time-dependent coefficients which can be solved using a numerical procedure. Here, a fourth order Runge–Kutta scheme was employed in order to solve these ODEs using ode45 algorithm in MATLAB. For the moving concentrated mass problem, the aforementioned procedure was employed for the simply supported beam of [18], and the efficiency was verified. The characteristics of the moving mass problem, solved in [18], are given in Table 1.

A comparison between deflection time histories of the beam at point $x_b = 7L_b/16$, obtained from numerical solution and [18] for speeds 3.06 and 7.59 (km/h) represents the qualification of the procedure (Fig. 3).

Table 1
Characteristics of the moving mass problem given in [18].

Mass distribution per unit length of the beam (kg/m)	1.847
Bending stiffness of the beam (Nm ²)	162.6
Length of the beam (m)	1.0515
Weigh of the moving mass (N)	4.952

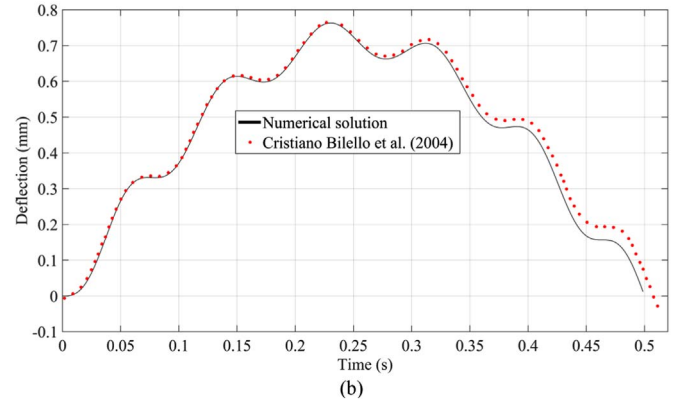
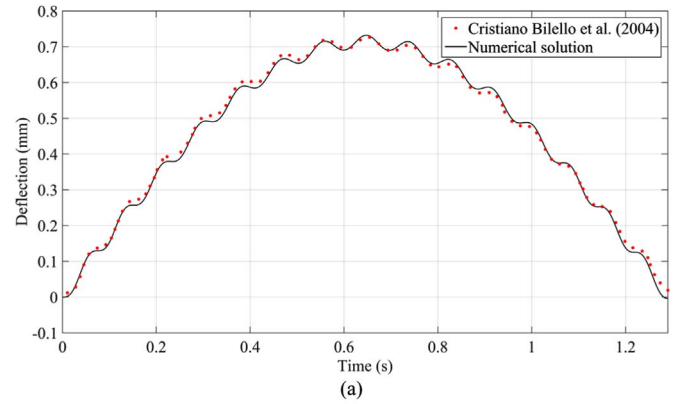


Fig. 3. Time histories of the beam deflection at point $x_b = 7L_b/16$ for speed equal to (a) 3.06 (km/h), and (b) 7.59 (km/h).

4. Modeling the piezoelectric cantilever beam energy harvester

A cantilever beam type piezoelectric energy harvester is considered in order to collect vibration energy from the bridge. Base-excited mechanical vibrations as a result of the bridge response to the moving mass are the source of input power for the harvester. The resonant frequency of the harvester is tuned to the fundamental eigen-frequency of the bridge, since speeds of the traversing vehicles are typically in a range that lower eigen-frequencies of the bridge will be excited the most [9].

The electromechanical modeling of cantilever piezoelectric energy harvesters can be found in the literature [19]. In this study, the power harvester is composed of an Euler–Bernoulli beam as a substrate, a tip mass and a single piezoelectric patch whose electrodes are connected to a changeable resistance (see Fig. 4). By using Hamilton's principle and taking only one mode shape into account [19], the coupled electro-mechanical governing equations of the SDOF harvester model can be derived as follows:

$$M_h \ddot{r}(t) + C_h \dot{r}(t) + K_h r(t) - \theta v(t) = -B_f \ddot{w}(x_b, t) \quad (22)$$

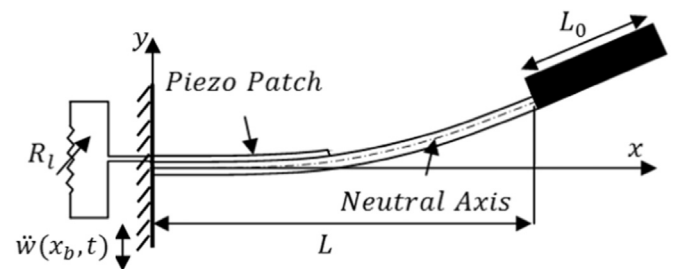


Fig. 4. Schematic diagram of the cantilevered beam type piezoelectric energy harvester.

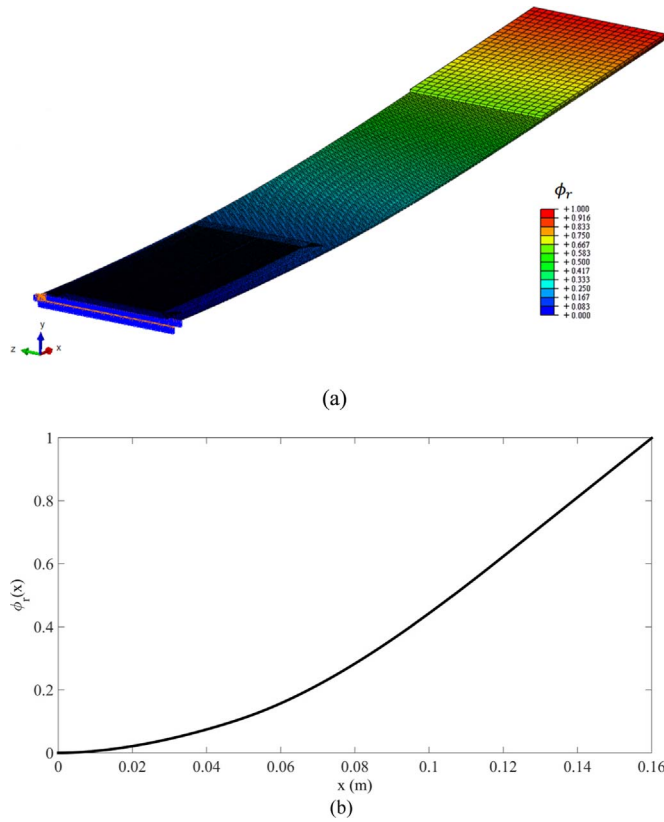


Fig. 5. (a) The harvester finite element model, and (b) fundamental mode shape of the harvester.

$$\theta \dot{r}(t) + C_p \dot{v}(t) + \frac{1}{R_l} v(t) = 0. \quad (23)$$

In Eqs. (22) and (23), $r(t)$ and $v(t)$ are generalized mechanical and electrical voltage coordinates, respectively. $\ddot{w}(x_b, t)$ is the harvester base acceleration resulting from the bridge vibrations under the moving mass and R_l is the electrical resistive load. It should be mentioned that the resonance frequency and the corresponding mode shape of the harvester can be calculated by using finite element method, since the material and the geometry are not constant along the harvester (see Fig. 5).

From the fundamental mode shape of the harvester the mechanical parameters M_h , K_h and B_f can be obtained as:

$$M_h = \int_0^L m \phi_r^2 dx + m_0 L_0 (\phi_r(L))^2 + m_0 L_0^2 \phi_r(L) \phi_r'(L) + [I_{zz} + m_0 L_0 (L_0^2 + h^2)] (\phi_r'(L))^2 \quad (24a)$$

$$K_h = M_h \omega_{1h}^2 \quad (24b)$$

$$B_f = \int_0^L m \phi_r dx + m_0 L_0 \phi_r(L) + \frac{1}{2} m_0 L_0^2 \phi_r'(L) \quad (24c)$$

where m is the mass per length distribution of the harvester beam and a function of x (axial beam coordinate, see Fig. 4). Parameters m_0 , L_0 , I_{zz} and h are the mass per length of the proof mass, the length of the proof mass, the rotational inertia of the proof mass around its center of gravity, and the distance of the center of gravity of the proof mass from the beam neutral axis, respectively. Parameter ϕ_r is the first mode shape function for the displacement of the cantilever beam and primes show spatial derivatives. ω_{1h} is the resonance frequency of the harvester (with short-circuit boundary condition), and is obtained from finite element method.

In (22) and (23), parameter C_h is a viscous damping coefficient and will be determined by experiment. Moreover, the coupling term θ and

the capacity C_p can be expressed as follows [13]:

$$\theta = -e_{31} w_p \left(\frac{t_p + 2d}{2} \right) \phi_r'(l_p) \quad (25)$$

$$C_p = \frac{\epsilon_{33}^S w_p l_p}{t_p} \quad (26)$$

where parameters e_{31} and ϵ_{33}^S are effective piezoelectric constant and absolute permittivity at constant strain for the piezoelectric patch, respectively, which are reduced for the plane-stress conditions. The poling direction is the 3-direction (y-direction in Fig. 4), and the axial direction is the 1-direction (x-direction in Fig. 4). Parameters l_p , w_p and t_p are the length, the width, and the thickness of the piezoelectric layer, respectively, while d is the distance of the neutral axis of the beam from the top surface of the substrate layer.

By transforming the governing Eqs. (22) and (23) from the time domain into the frequency domain the transfer function of the harvester can be written as:

$$H(\omega) = \frac{iB_f \theta \omega}{\left[\frac{K_h}{R_l} - \left(\frac{M_h}{R_l} + C_h C_p \right) \omega^2 \right] + i \left[\left(K_h C_p + \frac{C_h}{R_l} + \theta^2 \right) \omega - M_h C_p \omega^3 \right]} \quad (27)$$

This is the ratio between the complex voltage response and the complex input base acceleration. The voltage output and power output frequency response functions (FRFs) per base acceleration are sequentially obtained as follows:

$$\left| \frac{V}{A_B} \right| = \frac{B_f \theta \omega}{\sqrt{\left[\frac{K_h}{R_l} - \left(\frac{M_h}{R_l} + C_h C_p \right) \omega^2 \right]^2 + \left[\left(K_h C_p + \frac{C_h}{R_l} + \theta^2 \right) \omega - M_h C_p \omega^3 \right]^2}} \quad (28)$$

$$\left| \frac{P_{out}}{A_B^2} \right| = \frac{1}{2R_l} \frac{(B_f \theta \omega)^2}{\left[\frac{K_h}{R_l} - \left(\frac{M_h}{R_l} + C_h C_p \right) \omega^2 \right]^2 + \left[\left(K_h C_p + \frac{C_h}{R_l} + \theta^2 \right) \omega - M_h C_p \omega^3 \right]^2} \quad (29)$$

P_{out} shows the average power (per cycle) which is delivered to the resistor. The parameters V and A_B denote the voltage output amplitude and the acceleration amplitude of the harvester base, respectively.

The optimal electrical resistance and the optimal excitation frequency at which the maximum power is gained can be obtained by solving equations $\partial P_{out} / \partial R_l = 0$ and $\partial P_{out} / \partial \omega = 0$ simultaneously [12].

5. Parameter identification and model validation of the piezoelectric energy harvester

5.1. Experimental setup

The piezoelectric energy harvester is designed, fabricated, and tested (see Fig. 6(a)). The experimental setup and its schematic diagram are shown in Figs. 6(b), and (c), respectively. The harvester is designed with a resonant frequency of close to 13.5 Hz which is equal to the fundamental frequency of the considered bridge. The harvester is composed of a stainless steel substructure bonded with a Midé QP10N patch at its clamped end side, and an additional mass attached to the free end side.

The parameters of the harvester are given in Table 2.

By using the physical and geometric properties of the harvester as well as its fundamental mode shape function, system parameters are determined as represented in Table 3.

5.2. Experimental and analytical FRFs

In order to determine the linear electroelastic FRFs of the system, low-amplitude chirp excitation tests are carried out. The experimental

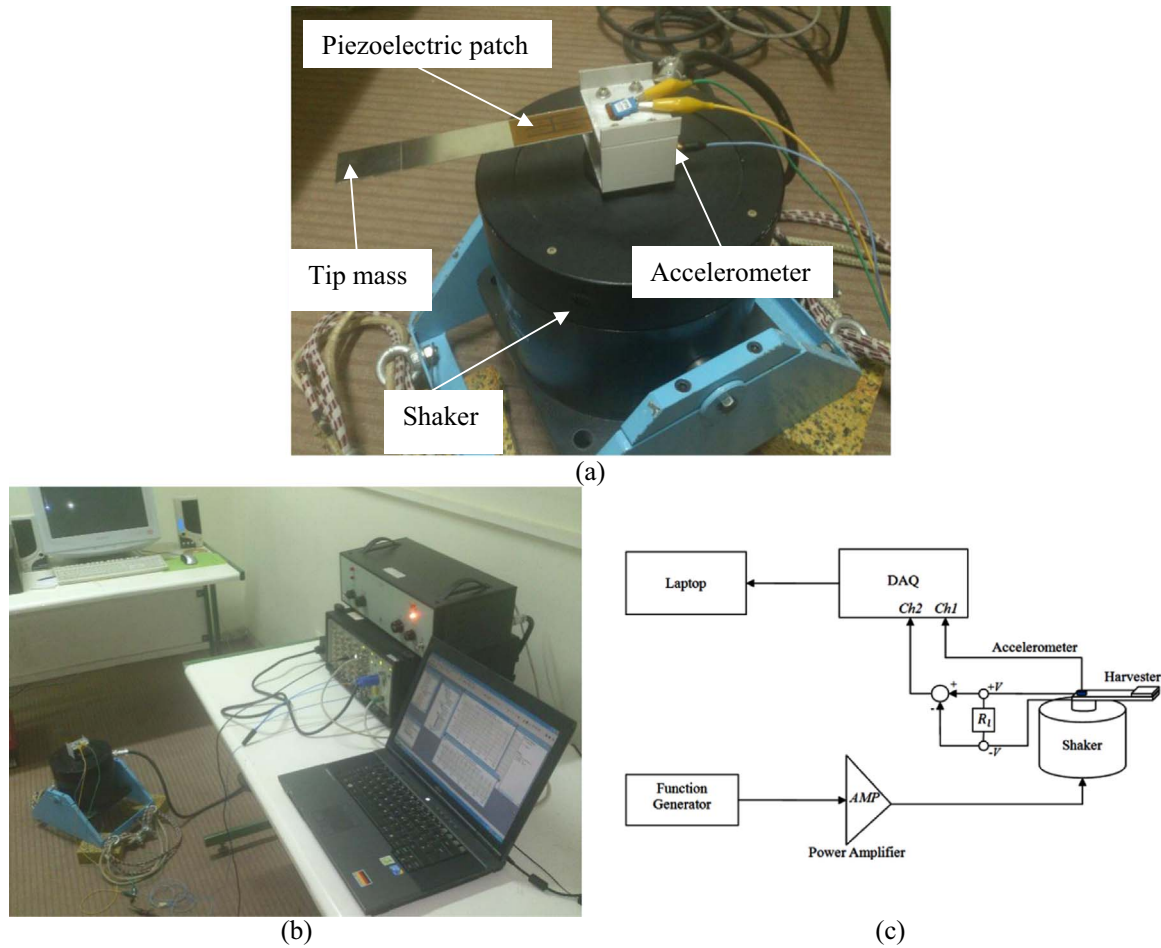


Fig. 6. Experimental setup, (a) the harvester, (b) measurement equipment, (c) schematic diagram of equipment.

Table 2
Physical and geometric properties of the harvester.

c_s	Substrate layer stiffness (GPa)	193
c_{11}^E	Piezoelectric layer stiffness (GPa)	61
ρ_s	Substrate layer density (kg m^{-3})	7515
ρ_p	Piezoelectric layer density (kg m^{-3})	7800
ρ_0	Proof mass density (kg m^{-3})	7515
L	Length of the substrate layer to starting of the tip mass (mm)	120
L_0	Length of the tip mass (mm)	40
l_p	Length of the piezoelectric layer (mm)	45.974
w_s	Width of the substrate layer (mm)	28
w_p	Width of the piezoelectric layer (mm)	20.574
w_t	Width of the tip mass (mm)	28
t_s	Substrate layer thickness (mm)	0.5
t_p	Piezoelectric layer thickness (mm)	0.381
t_t	Tip mass thickness (mm)	1
ϵ_{33}^S	Absolute permittivity (F m^{-1})	$1451\epsilon_0$
ϵ_0	Vacuum permittivity (F m^{-1})	8.854×10^{-12}
d_{31}	Strain constant (C N^{-1})	-190×10^{-12}
e_{31}	Stress constant (C m^{-2})	-11.6
ζ	The harvester mechanical damping ratio	0.04

Table 3
Lumped model parameters of the harvester.

M_h (g)	K_h (N m^{-1})	C_h (N sm^{-1})	θ (N V^{-1})	B_f (g)	C_p (nF)
7.3	51.81	0.05	5.85×10^{-5}	10.5	45.34

FRFs and those corresponding coherence functions of the system regarding the open-circuit and short-circuit conditions are represented in Figs. 7 and 8, respectively. Note that for the frequency range of measurement, ultimate precision of the data acquisition system is employed; that is to say the frequency resolution is set equal to 0.125 (Hz). As the FRFs show, due to the low contribution of the piezoelectric coupling term in the overall structural stiffness, the eigen-frequencies of the two electrical boundary conditions are very close to each other. The coherence functions of voltage output is unity over the frequency range; however, due to the AC noise in the test environment wires, the functions dramatically decrease at 50 (Hz).

The differences between the first and second resonance frequencies of the harvester (13.5 (Hz) and 96.6 (Hz), respectively) are high enough that one can conclude higher modes have negligible contribution in the system responses. As a result, single mode approximation is an acceptable approximation in the prediction of the harvester responses due to low frequency excitations, especially as the excitations in our study have frequencies below 20 (Hz).

The parameters of the harvester device are so that the optimal excitation frequency, at which maximum power can be harvested, is close to the fundamental frequency of the harvester ($\omega_{1h} = \sqrt{K_h/M_h}$) [12]. Thus, the harvester is excited with a sinusoidal acceleration with a frequency of 13.5 (Hz) (resonance frequency) and an amplitude of 2 (m/s^2) at the base with varying resistive loads. Predicted results from modeling are graphically demonstrated in Figs. 9(a) and (b) using lines while experimental results are presented by dots. In the test, the RMS values of voltage output are measured at various discrete electrical load resistances ranging from 30 k Ω to 850 k Ω . Consequently, the power output at each electrical load resistance is calculated using $P_{\text{out}} = v_{\text{rms}}^2/R_l$.

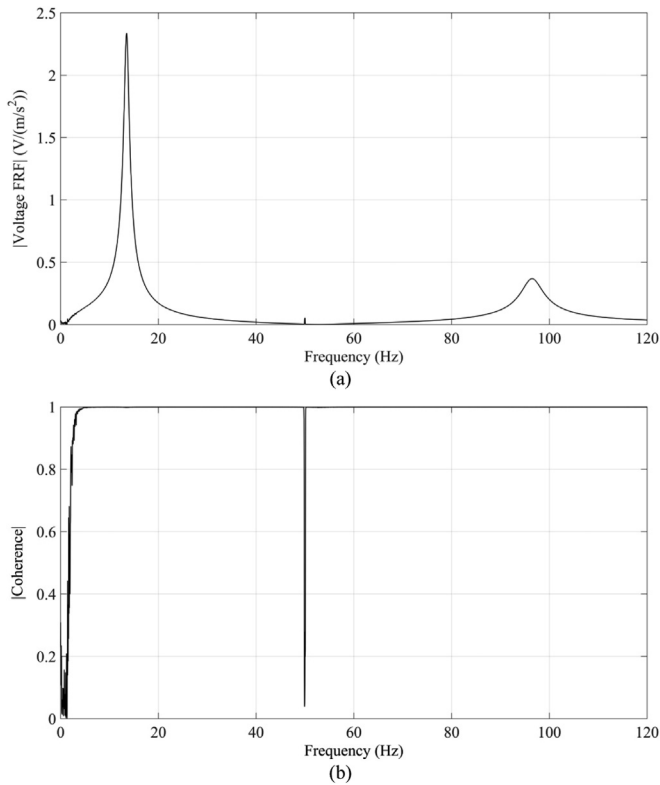


Fig. 7. (a) The harvester Voltage output FRF, and (b) the corresponding coherence function (open-circuit condition).

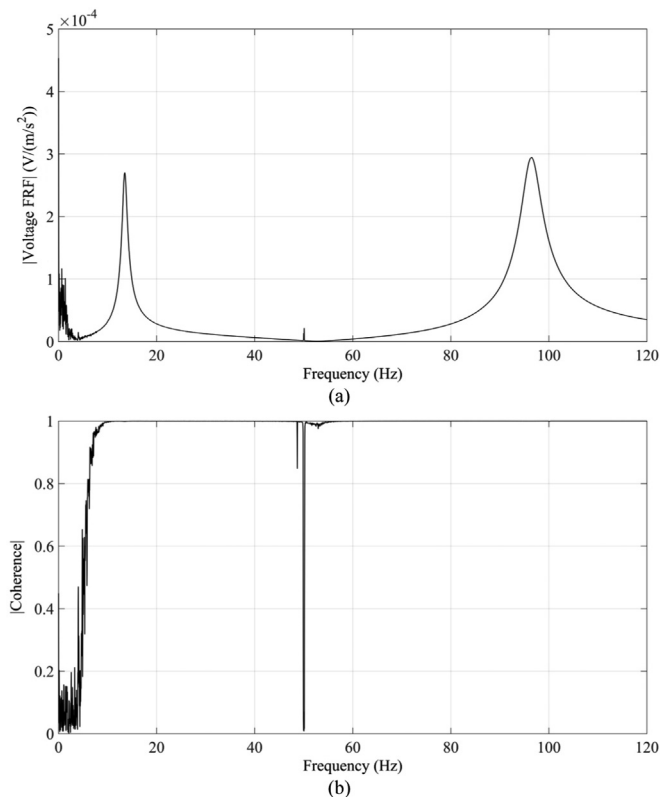


Fig. 8. (a) The harvester voltage output FRF, and (b) the corresponding coherence function (short-circuit condition).

Overall, theory is in good agreement with experimental results at various electrical loads. The discrepancy between experimental and theoretical results may be attributed to some sources. Firstly, as

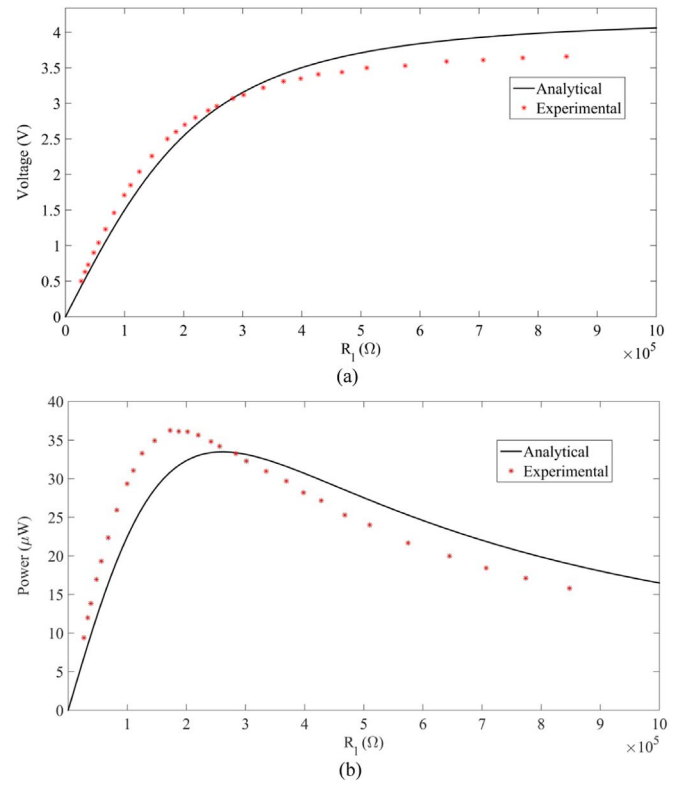


Fig. 9. Variation of (a) RMS value of the voltage output (b) the power output versus load resistance for excitation at the resonance frequency.

mentioned, the operating frequency at which the results are obtained is equal to the resonance frequency of the energy harvester. Nonlinearity which is arisen from large deflection of the energy harvester due to vibration at resonance frequency might lead to error, while in the theory the model of harvester is considered linear and nonlinearity effects are neglected. As it was shown in [20] as further away from resonance, the closer the model is to the experimental results. The second source of discrepancy may be attributed to the resistors at which the RMS values of voltages output are measured. These resistors have 2% tolerance and might lead to systematic errors in obtained results. Finally, as can be seen in Fig. 9(a), experimental results of the RMS values of the generated voltages agree better with the theoretical predictions as compared with curves in Fig. 9(b). This is mainly because the RMS values of voltage output is squared, when the power output at each electrical load resistance is calculated, and thus, the differences between the RMS values of the measured voltage and predicted one have become more prominent.

The optimal resistive load at which maximum power is extracted is found to be about 200 (kΩ) (see Fig. 9(b)).

The comparison of the voltage output FRFs calculated theoretically (Eq. (28)) and experimentally with presence of the optimal load resistance is shown in Fig. 10. As can be seen, the analytical FRF is in good agreement with the experimental one.

To this point, a model for a bridge under concentrated moving mass was introduced. The governing equations were derived and the obtained results were compared with those for a real bridge in literature. Next, the equations of motion for a bridge under distributed travelling mass were extracted. Also, an analytical model for the harvester was presented and then validated by some experiments. It was shown that the model can predict the electromechanical characteristics of the harvester with a good degree of accuracy. In the next section, the acceleration of a point located at the mid-span of the bridge will be calculated numerically. The mid-span acceleration time history will be computed for both concentrated and distributed masses. The

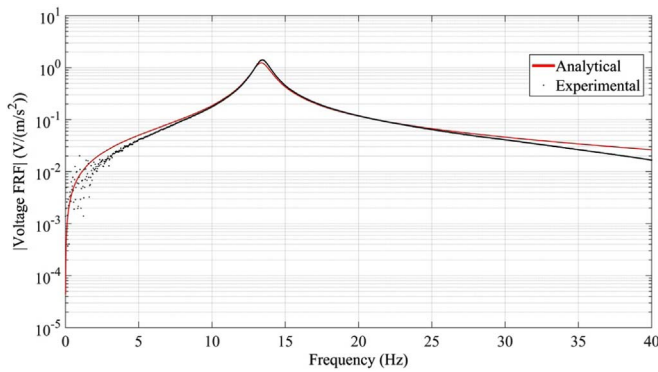


Fig. 10. The harvester voltage output FRF with optimal resistive load.

obtained acceleration time history will then be used as a base excitation signal to the harvester.

6. Energy harvesting from a bridge vibration

In this section, the maximum harvestable energy from a bridge vibration, resulting from traversing two different types of masses as vehicle models, is investigated within two numerical examples. These two examples are:

1. Traversing of a concentrated mass
2. Traversing of a distributed mass with the length equal to half of the bridge length

Three different vehicle speeds ranging from 20 to 30 (m/s) with an interval of 5 (m/s) are adopted for each of the two aforementioned examples. In this study, the responses of the bridge to the moving masses are calculated by only considering the fundamental mode shape of the bridge. Also, the harvester is tuned to this mode shape. Therefore, the optimum location wherein the harvester should be attached to the bridge in order to extract the maximum energy is at the middle of the bridge in which the first mode shape of the bridge has maximum amplitude [10]. Note that since the harvester mass is negligible compared to that of the bridge, the bridge response will not be affected by the harvester mass. It should be mentioned that in both of these two examples the voltage output of the harvester is calculated only when the masses are on the bridge i.e. from the time the vehicle arrives to the bridge until it departs from the bridge completely.

In order to validate the voltage output results, the acceleration signals which are derived from solving the moving mass problems in each example are replayed on the shaker to simulate the bridge vibrations and the experimental results are compared with theoretical ones.

Furthermore, to obtain the time history of the voltage output theoretically, the harvester governing equations are transferred to several first-order differential equations and the numerical solution of the response of the system is calculated in the time domain using ode45 algorithm in the MATLAB development environment.

7. Numerical examples

A steel bridge is the case of study for energy harvesting in this investigation. The specifications of the bridge are given in the Table 4. The specifications of the bridge are kept the same for both examples.

7.1. Traversing of a concentrated mass

In this example, energy harvesting problem for a vehicle, modeled as a 5000 (kg) concentrated mass traversing the bridge, is solved for three different speeds and results are represented within four figures

Table 4
Specifications of the bridge.

m_b	Mass distribution per unit length (kg/m)	3730
ζ_{1b}	Mechanical damping ratio	0.02
E_b	Young's modulus (GPa)	210
I_b	Second moment of area (m ⁴)	0.47
L_b	Length (m)	16
$\omega_{1b}/2\pi$	Fundamental frequency (Hz)	13.5

for each speed. Also, it is assumed that, the speed of the mass remains constant while traversing the bridge. Fig. 11, parts (a) and (b) show the time histories of the deflection and acceleration of the mid-span of the bridge while the concentrated mass traverses the bridge, respectively. Fig. 11(c) represents the power spectral density of the acceleration response of the bridge at the mid-span, and finally Fig. 11(d) shows the comparison between theoretical and experimental output voltage of the harvester in presence of optimal resistive load as a result of the bridge vibrations caused by the moving mass. Note that in Fig. 11 all results are shown for the time span when the mass is on the bridge, i.e. from the time the vehicle arrives to the bridge until it departs from the bridge completely.

As seen in the power spectral density diagrams corresponding to the acceleration response of the mid-span of the bridge for each speed, there are two dominant frequencies in each power spectral density diagram. The lower frequency corresponds to forced vibration frequency of the bridge due to the motion of the concentrated mass and the higher one is the fundamental frequency of the bridge. As shown in Fig. 11(c) the excitation frequency increases as the speed of the moving mass increases, while the fundamental frequency of the bridge is constant. Also, as these power spectral density diagrams show, the second peak or resonant frequency of the bridge has larger amplitude compared to the first peak or excitation frequency of the bridge. As a consequence, in order to extract maximum power from bridge vibrations, one should tune the harvester resonance frequency to the first natural frequency of the bridge as is done in this study. Furthermore, as the speed of the moving mass increases, the amplitudes of both lower and higher dominant frequencies in the PSD diagrams rise. Similar trends observe in the amplitudes piezoelectric patch voltage output. It is noteworthy that after the mass departs from the bridge, the bridge will vibrate freely with its fundamental frequency of 13.5 Hz.

The discrepancy between time histories of the theoretically predicted voltage output and the voltage output derived from experiment is mostly due to the incapability of the shaker in excitations with frequencies less than 5 Hz. Therefore, the excitations produced by the shaker do not contain frequencies below 5 Hz; while, the acceleration signals that are given to the shaker by function generator contain frequencies below 5 Hz. However, since the resonance frequency of the harvester is tuned to the resonance frequency of the bridge (i.e. 13.5 Hz) the discrepancy between the two aforementioned time histories is low as the maximum amplitude of the harvester response is at frequency equal to 13.5 Hz.

7.2. Traversing of a distributed mass with the length equal to half of the bridge length

Similar to the previous example, in this example energy harvesting problem for a moving distributed mass with the length equal to half of the bridge length is considered. Again, the problem is solved for three different speeds and results are represented within four figures for each speed. The mass per unit length of the distributed mass is considered one third of the bridge mass per unit length and the rigidity modulus of the distributed mass is assumed to be zero. In Fig. 12, parts (a) and (b) show the time histories of the deflection and acceleration of the mid-span of the bridge while the distributed mass traverses the bridge. Fig. 12(c) denotes the power spectral density of the acceleration

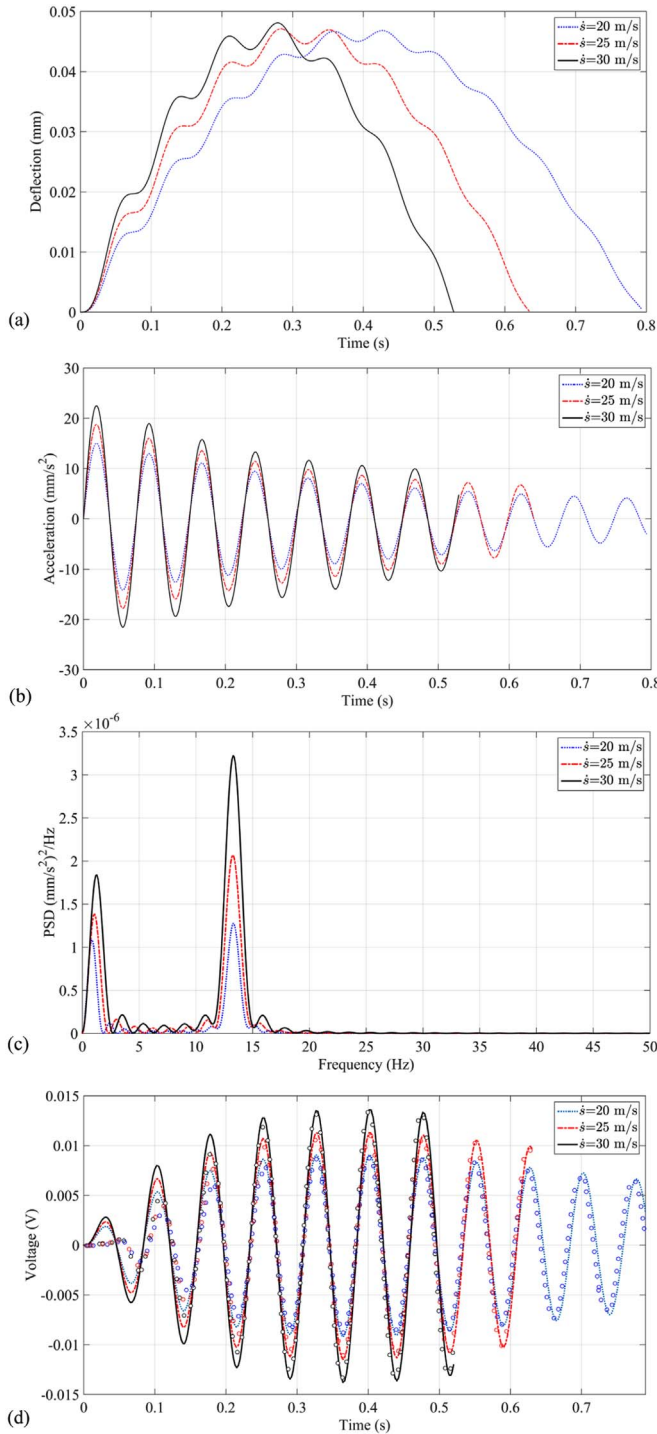


Fig. 11. Results of energy harvesting for a moving concentrated mass passing on a bridge. (a) Time history of deflection for three different speeds of concentrated mass at mid span of the beam ($x_b=L_b/2$) (b) Time history of acceleration for three different speeds of concentrated mass at mid span of the beam ($x_b=L_b/2$) (c) PSD of acceleration for three different speeds of concentrated mass at mid span of the beam ($x_b=L_b/2$) (d) Voltage output of piezoelectric patch versus time for three different speeds of concentrated mass (Solid lines are the theoretical predictions and circles are the experimental results).

response of the bridge at the mid-span, and finally Fig. 12(d) depicts the comparison between theoretical and experimental output voltage of the harvester in the presence of optimal resistive load as a result of the bridge vibrations caused by the moving distributed mass. Note that in Fig. 12 all results are displayed from the time that the right corner of the vehicle arrive the bridge until its left corner leaves the bridge completely.

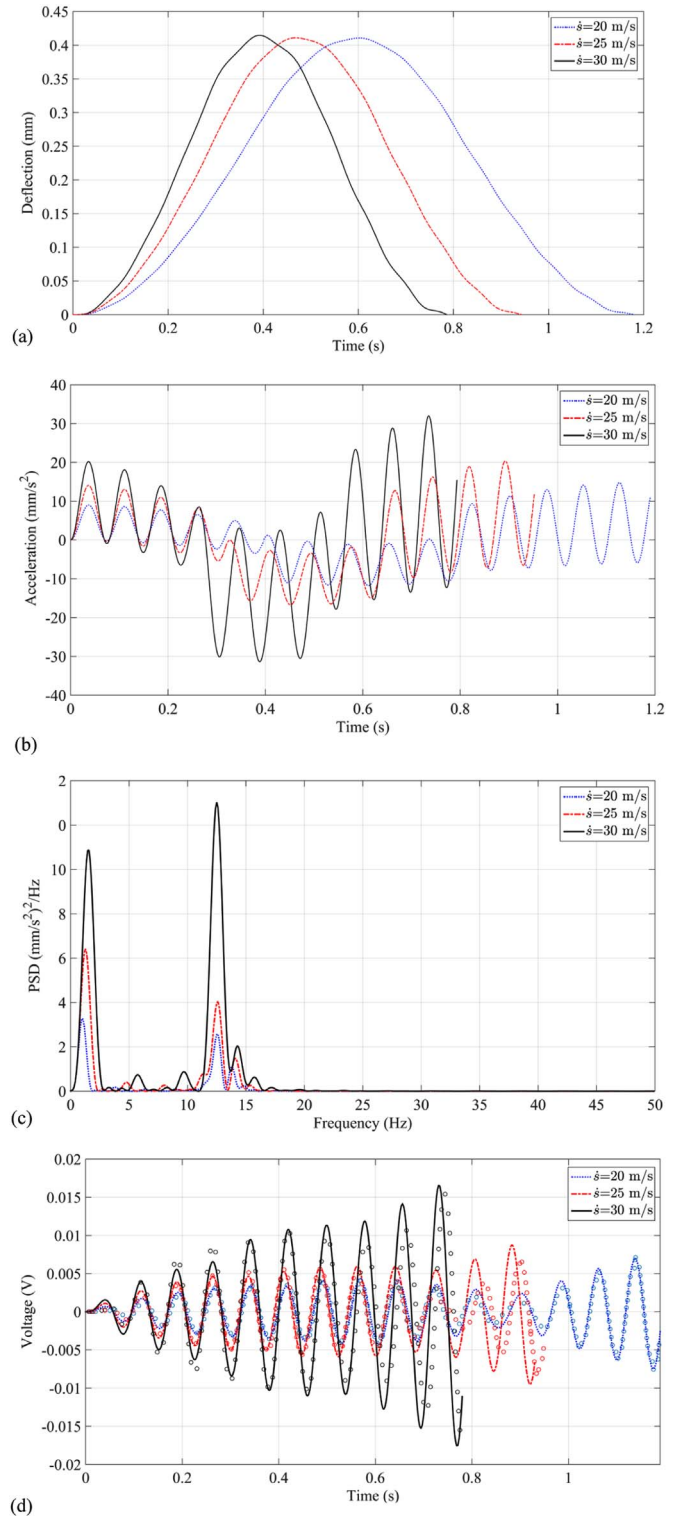


Fig. 12. Results of energy harvesting for a moving distributed mass passing on a bridge. (a) Time history of deflection for three different speeds of distributed mass at mid span of the beam ($x_b=L_b/2$) (b) Time history of acceleration for three different speeds of distributed mass at mid span of the beam ($x_b=L_b/2$) (c) PSD of acceleration for three different speeds of distributed mass at mid span of the beam ($x_b=L_b/2$) (d) Voltage output of piezoelectric patch versus time for three different speeds of distributed mass (Solid lines are the theoretical predictions and circles are the experimental results).

As seen in the power spectral density diagrams corresponding to the acceleration response of the mid-span of the bridge for each speed, similar to the moving concentrated mass problem, there are two dominant frequencies in each power spectral density diagram. The

Table 5

Root mean square values of voltage output of travelling masses with different lengths and same masses for speed equal to 30 (m/s).

Type of travelling 5000 (kg) mass	Root mean square of voltage output (mV)
Concentrated mass ($L_d \rightarrow 0$)	8.030
$L_d = L_b/4$	1.821
$L_d = L_b/3$	1.643
$L_d = L_b/2$	1.591
$L_d = 3L_b/4$	0.876
$L_d = L_b$	0.356

lower frequency corresponds to the excitation frequency of forced vibration of the bridge due to motion of the distributed mass and the upper one is the fundamental frequency of the bridge. Similar to the case of concentrated mass, the excitation frequency increases as speed of the moving distributed mass increases, while the fundamental frequency of the bridge is constant. Contrary to the moving concentrated mass problem, in this example, the resonant frequency of the bridge has a lower amplitude compared to the excitation frequency of the bridge, except at the speed of 30 (m/s). However, in this example the harvester resonance frequency is tuned to the first natural frequency of the bridge as well, since unlike the bridge excitation frequency, the bridge fundamental frequency is constant and independent from the distributed mass speed. Similar to the moving concentrated mass problem, as speed of the moving distributed mass increases, the amplitudes of the both lower and upper dominant frequencies in PSD diagrams rise and likewise an increase in the amplitudes of the time histories of voltage output occurs.

A theoretical investigation is carried out in order to find the effect of the length of the moving masses on the amount of harvested power. To this end, root mean squares of voltage output resulted by motion of bodies with different lengths but same masses 5000 (kg) at speed of 30 (m/s) are obtained. The results are presented in Table 5. As shown in Table 5, by increasing of the length of the moving masses, the RMS values of voltage output and consequently the power output will decrease. This is mainly due to the fact that the bridge amplitude of vibration for distributed masses is less than the concentrated ones.

8. Electrical circuits for energy extraction

When a piezoelectric energy harvester is connected to a simple electrical load circuit, the electrical damping force produced by piezoelectric element is often below the optimal value in which the power output is the maximum [21]. This is mainly because of the low electromechanical coupling coefficients, which can be achieved [22,23]. The maximum damping for a piezoelectric device, when a simple resistive or rectifying load is used, is small. Consequently, diverse load circuits have been proposed to overcome this limit by modification of the electrical damping force and various types of those can modify the electrical damping by different values. Among the various circuits, some types can run a charging current through a storage element such as a rechargeable battery or capacitor to provide a dc voltage, while the other types provide a time-varying voltage.

Different realistically achievable types of power-extraction circuits have been introduced for piezoelectric energy harvesters, which among those the purely load resistance and bridge rectifier with a smoothing capacitor [24] are the most common. The maximum power output of the bridge rectifier circuit is less than that of purely resistive load; however, bridge rectifier circuit is more useful as almost all electronic loads require a dc input. In addition, for the bridge rectifier circuit, the open-circuit voltage output of the piezoelectric element must be large enough to overcome the diode on-stage voltage drops. However, In the case of low-amplitude vibrations, this condition may not be achievable.

Purely resistive load is the simplest circuit for extracting power and was used as a base case for comparison with the other circuits. To

extract more power, more complex power-extraction circuits can be used. The single-supply pre-biasing circuit has the potential to perform best at all operating conditions. This circuit gives a dc output and provides a condition in which the open-circuit voltage does not need to overcome diode drops. Thus, it is useful in the case of low input excitation, where the open-circuit voltage is small. It was shown in [25] that the single-supply pre-biasing power output is about 16 times more than that of optimal resistive load and also has the highest power density compared to the other circuits with dc outputs. However, it requires control circuitry that makes the design of the circuit complex. In contrast, bridge rectifier circuit is simple and hence more reliable. Furthermore, there are various commercial Integrated Circuits (ICs) with energy harvesting applications that can be utilized to extract and store the harvested energy [26]. These ICs can easily adapt to a wide range of voltage and power inputs and outputs.

9. Conclusions

This paper focused on harvesting of energy using a cantilever beam type piezoelectric energy harvester from a bridge vibration. First, the problem of moving mass travelling on a simply supported beam was considered.

For heavy and high speed masses traversing over a beam, the travelling mass inertial effects should be taken into account.

To validate the model presented for a concentrated mass moving over a bridge, the obtained results were compared to those available in the literature. The results revealed little discrepancy between those from the proposed model with the data presented in [18].

In the formulation of a distributed moving mass over a beam, the length of the moving mass is of importance, which divides the problem into three separate steps. In each step, the governing equations of motion of the system are different. If the length of the moving mass is less than the length of the beam, three different steps and formulations should be considered, namely entrance, main and exit steps.

The electromechanical model for the cantilever piezoelectric energy harvester which is composed of an Euler–Bernoulli beam as a substrate, a tip mass and a single piezoelectric patch was derived using Hamilton's principle. It was found that due to variable geometry of the harvester along its length, it is better to compute the mode shapes of the harvester using the finite element method. The first natural frequency of the harvester was found to be around 13.5 (Hz) which is close to the fundamental mode of the bridge.

The measured eigen-frequencies of the harvester for open and short-circuit boundary conditions are very close to each other. This indicates that the piezoelectric coupling term has no significant effect on the overall stiffness of the structure.

The experimental results showed that the optimal load resistance at the resonance frequency of the harvester is about 200 (k Ω).

The measured voltage induced in the harvester due to the moving mass follows properly the voltage calculated by the analytical model. This verifies that the proposed model is of good accuracy and can be used in design of practical harvester for the bridge.

For the case of concentrated mass traversing the beam, it was found that by increasing the moving mass speed, the maximum voltage produced by the harvester is increased. The increase in voltage is almost proportional to the speed increment.

For the case of distributed mass, the voltage output of piezoelectric patch has variations through time which are caused by the different stages of the mass on the beam, namely the entrance, main and exit steps. The results also showed that the maximum voltage occurs at the exit step of the distributed travelling mass.

The obtained results also indicate that the RMS of piezoelectric harvester voltage output has the largest value for a concentrated mass. As the mass spread over the beam, the RMS of generated voltage output will decrease significantly.

References

- [1] Ko JM, Ni YQ. Technology developments in structural health monitoring of large-scale bridges. *Eng Struct* 2005;27(12):1715–25.
- [2] Lynch JP, Loh KJ. A summary review of wireless sensors and sensor networks for structural health monitoring. *Shock Vib Dig* 2006;38(2):91–130.
- [3] Sazonov, E, Janoyan, K, Jha, R. Wireless intelligent sensor network for autonomous structural health monitoring. In: *Smart Structures and Materials*. International Society for Optics and Photonics; 2004. p. 305–14.
- [4] Mak, N.H. and Seah, W.K., 2009, May. How long is the lifetime of a wireless sensor network?. In: *Proceedings of the IEEE international conference on advanced information networking and applications*; 2009. p. 763–70.
- [5] Harb A. Energy harvesting: state-of-the-art. *Renew Energy* 2011;36(10):2641–54.
- [6] Halvorsen E. Energy harvesters driven by broadband random vibrations. *J Micro Syst* 2008;17(5):1061–71.
- [7] Rytter, A. *Vibrational based inspection of civil engineering structures* (Doctoral dissertation, unknown); 1993.
- [8] Cook-Chennault KA, Thambi N, Sastry AM. Powering MEMS portable devices—a review of non-regenerative and regenerative power supply systems with special emphasis on piezoelectric energy harvesting systems. *Smart Mater Struct* 2008;17(4):043001.
- [9] Williams, CB, Pavic, A, Crouch, RS, Woods, RC. Feasibility study of vibration-electric generator for bridge vibration sensors. In: *SPIE proceedings series*. Society of Photo-Optical Instrumentation Engineers; 1998. p. 1111–17.
- [10] Ali SF, Friswell M, Adhikari S. Analysis of energy harvesters for highway bridges. *J Intell Mater Syst Struct* 2011. [1045389×11417650].
- [11] Galchev TV, McCullagh J, Peterson RL, Najafi K. Harvesting traffic-induced vibrations for structural health monitoring of bridges. *J Micromech Microeng* 2011;21(10):104005.
- [12] Peigney M, Siegert D. Piezoelectric energy harvesting from traffic-induced bridge vibrations. *Smart Mater Struct* 2013;22(9):095019.
- [13] Zhang Y, Cai SC, Deng L. Piezoelectric-based energy harvesting in bridge systems. *J Intell Mater Syst Struct* 2014;25(12):1414–28.
- [14] Michaltsos GT. The influence of centripetal and coriolis forces on the dynamic response of light bridges under moving vehicles. *J Sound Vib* 2001;247(2):261–77.
- [15] Meirovitch L. *Elements of vibration analysis*, 2nd ed.. New York: McGraw-Hill; 1986.
- [16] Esmailzadeh E, Ghorashi M. Vibration analysis of beams traversed by uniform partially distributed moving masses. *J Sound Vib* 1995;184(1):9–17.
- [17] Frýba L. *Vibration of solids and structures under moving loads*, 1. Springer Science & Business Media; 2013.
- [18] Bilello C, Bergman LA, Kuchma D. Experimental investigation of a small-scale bridge model under a moving mass. *J Struct Eng* 2004;130(5):799–804.
- [19] Sodano HA, Park G, Inman DJ. Estimation of electric charge output for piezoelectric energy harvesting. *Strain* 2004;40(2):49–58.
- [20] Kim M, Hoegen M, Dugundji J, Wardle BL. Modeling and experimental verification of proof mass effects on vibration energy harvester performance. *Smart Mater Struct* 2010;19(4):045023.
- [21] Mitcheson PD, Green TC, Yeatman EM, Holmes AS. Architectures for vibration-driven micropower generators. *J Micro Syst* 2004;13(3):429–40.
- [22] Al Ahmad M, Alshareef HN. Modeling the power output of piezoelectric energy harvesters. *J Electron Mater* 2011;40(7):1477–84.
- [23] Liang J, Liao WH. Energy flow in piezoelectric energy harvesting systems. *Smart Mater Struct* 2010;20(1):015005.
- [24] Ottman GK, Hofmann HF, Bhatt AC, Lesieutre GA. Adaptive piezoelectric energy harvesting circuit for wireless remote power supply. *IEEE Trans Power Electron* 2002;17(5):669–76.
- [25] Dicken J, Mitcheson PD, Stoianov I, Yeatman EM. Power-extraction circuits for piezoelectric energy harvesters in miniature and low-power applications. *IEEE Trans Power Electron* 2012;27(11):4514–29.
- [26] (<http://www.digikey.com/en/product-highlight/a/advanced-linear-devices/eh300-eh301-series-energy-harvesting>); 2016 [accessed on 20.05.16].